in the original micrographs[5] and can thus be compared with the reconstructed image.

Acknowledgment. This work has been supported by the Deutsche Forschungsgemeinschaft, Sonderforschungsbereich 262.

Registry No. Hexapentoxytriphenylene, 69079-52-3.

References and Notes

(1) Durst, H.; Voigt-Martin, I. G. *Makromol. Chem., Rapid Commun.* **1986**, *7*, 785.
(2) Voigt-Martin, I. G.; Durst, H. *Liq. Cryst.* **1987**, *2*(5), 585.
(3) Voigt-Martin, I. G.; Durst, H. *Liq. Cryst.* **1987**, *2*(5), 601.
(4) Voigt-Martin, I. G.; Durst; H.; Reck, B.; Ringsdorf, H. *Macromolecules* **1988**, *21*, 1620.
(5) Voigt-Martin, I. G.; Durst, H. *Macromolecules*, in press.
(6) Klug, A.; de Rosier, D. J. *Nature (London)* **1966**, *212*, 29.
(7) Taylor, C. A.; Lipson, H. *Optical Transforms*; Bell: London, 1964.
(8) Voigt-Martin, I. G.; Mijlhoff, F. C. *J. Appl. Phys.* **1976**, *47*, 3942.
(9) Pratt, N. K., Ed. *Digital Image Processing*; Wiley: New York, 1978.
(10) Wahl, F. M. *Digitale Bildsignalverarbeitung*; Springer-Verlag: Berlin, 1984.
(11) Krug, H.; Holoubek, J.; Fischer, E. W. *Colloid Polym. Sci.* **1987**, *265*, 779.
(12) Champeney, D. C. *Fourier Transforms and their Physical Applications*; Academic: New York, 1973; p 72.
(13) Voigt-Martin, I. G.; Brzezinski, V.; Durst, H.; Kreuder, W.; Ringsdorf, H., submitted for publication in *Nature (London)*.
(14) Tietz, R. *J. Microsc. Spectrosc. Electron.* **1986**, *11*, 65.
(15) Padere, P.; Revol, J. F.; Nguyen, L.; Manley, R. St. J. *Ultramicroscopy* **1988**, *25*, 69.

NMR Imaging of Elastomeric Materials

C. Chang and R. A. Komoroski*

Departments of Radiology, Pathology, and Biochemistry, University of Arkansas for Medical Sciences, Little Rock, Arkansas 72205. *Received March 3, 1988; Revised Manuscript Received June 28, 1988*

ABSTRACT: In order to establish the utility of NMR imaging for certain materials science applications, we have examined a number of elastomeric systems of similar glass transition temperature but differing chain segmental mobilities. As expected, the quality of the images is highly dependent on chain segmental mobility. Usable hydrogen images were obtained at ambient temperatures on two commercial imagers in reasonable times (one half-hour to overnight) for bulk *cis*-polybutadiene, natural rubber, and a cured, carbon-black-filled *cis*-polybutadiene. For typical 2D FT imaging where a spin echo is detected, image quality is, as expected, highly dependent on the relative values of T_2, the spin–spin relaxation time, and TE, the time to echo. Polyisobutylene, a rubber with the same T_g as natural rubber, but a $T_2 < 1$ ms, gave no image under the same conditions as for the other polymers. The polymers also were imaged by using a gradient–echo sequence. It appears that the gradient–echo sequence, which is sensitive to T_2^*, may be better than the spin–echo sequence, which is sensitive to T_2, for detection of defects such as voids, gaps, or small foreign particles in elastomers. This results from a magnification effect caused by magnetic susceptibility differences at the void surface. A crude resolution test was performed by using the spin–echo sequence on multiple sheets of cured, filled *cis*-polybutadiene separated by NMR-transparent spacers of variable width. Features as small as 0.07 mm could be detected even though the pixel size was 0.47 mm.

Introduction

Nuclear magnetic resonance imaging has evolved into an important diagnostic modality in clinical medicine over the last 10 years.[1,2] Although the technique can be performed in a number of ways, in every case it provides a picture of NMR signal intensity as a function of location (in one, two, or three dimensions) in an object. Depending on technique details, the location-dependent NMR signal is a function of local spin concentration and local spin–lattice (T_1) and spin–spin (T_2) relaxation times. As for typical high-resolution NMR spectroscopy, NMR imaging detects only the liquid or liquidlike components in the human body—mainly water and fat.

Whereas the clinical applications of NMR imaging have developed quite rapidly, applications in materials and polymer science have been slow to appear. This is due in part to the fact that commercial NMR imaging equipment suitable for such studies has become available only recently. It also arises from the more or less well founded belief that most important applications in materials science involve rigid solids, which cannot be studied by using standard equipment. Nevertheless, a number of nonmedical applications of NMR imaging has appeared. The majority of these reports deals with diffusion of liquids through rock,[3-11] wood,[12-15] or polymers.[16-19] Suits and White have imaged ionic distribution[20] and temperature profile[21] in solid ionic substances.

Efforts are currently underway on the development of NMR imaging techniques for rigid solids.[20-33] Solids pose formidable problems for standard NMR imaging techniques. The spread of frequencies imposed by the gradient forming the image must be larger than the linewidth. Typical solid-state proton line widths are on the order of 20 kHz, a value that precludes NMR imaging of rigid solids using standard gradient strengths of about 1–2 G/cm. Among the approaches being tried for rigid solids are line narrowing by multiple-pulse,[28,32] rotating-frame magic-angle,[30] laboratory-frame magic angle,[33] solid echo,[31] and heteronuclear-decoupling[25] techniques, multiple-quantum NMR to magnify the effect of the field gradient,[24,26] combined multiple-pulse sequences and radio-frequency (rf) field gradients,[29] and incrementing the field gradient during a fixed evolution time.[27] In addition, instrument manufacturers are beginning to provide systems with more powerful gradients, from 20 to 200 G/cm or greater.[34,35] For the most part these systems are geared to obtaining high-resolution NMR images of small but not necessarily rigid objects. Additional development work is necessary before the above and related techniques see widespread use for imaging truly rigid solids in materials or polymer

0024-9297/89/2222-0600$01.50/0

science. So far, these techniques have been demonstrated primarily on solids of relatively high molecular mobility, such as adamantane and hexamethylbenzene. However, images of polycarbonate have recently been displayed.[33]

It has been known for some time that high-resolution NMR spectra, both of ^1H and ^{13}C, can be obtained for bulk polymers well above their glass transition temperature T_g. A significant amount of high-resolution NMR work has appeared on such systems.[36] The quality, as reflected in the resonance line widths, of the high-resolution spectrum of a bulk, rubbery polymer depends to a large extent on the rate, amplitude, and anisotropy of chain segmental mobility at the temperature of interest. Typical proton NMR line widths for rubbery polymers at about 100 °C above T_g are in the range of about 100–2000 Hz. Thus molecular mobility has averaged the spin dipolar interactions significantly from the rigid case, but not to values typical for liquids in an imaging setting (10–50 Hz). The degree of line narrowing can be sufficient for imaging by standard techniques.

Rothwell and Gentempo[17] first demonstrated this by obtaining an image of an unspecified polymer in a composite "sandwich" at a temperature about 80 °C above T_g, which was given as 100 °C. The image of a sample of synthetic *cis*-polyisoprene at room temperature has been reported.[19] In their work applying multiple-pulse line narrowing to imaging, Chingas et al.[28] reported an NMR image of a section of neoprene (polychloroprene) hose. No details on NMR imaging of elastomers were explored in any of the above reports.

It is likely that the initial applications of NMR imaging in the science of polymeric materials will be found in heterogeneous, liquid–solid systems (in which case the liquid components will be imaged), in elastomeric systems (filled and/or cured) and composites, and perhaps in semicrystalline polymers where T_g is relatively low. In order to define more clearly the current limits of utility of certain types of commercially available equipment for applications of NMR imaging to materials or polymer science, we have examined at ambient temperature a number of elastomeric systems of similar T_g's but differing chain segmental mobilities. Both pure amorphous resins and cross-linked, filled materials are studied. Two imaging sequences which are sensitive to different NMR parameters are used on two different pieces of equipment. A crude resolution test is performed and used to demonstrate the level of information readily obtainable on available equipment.

Experimental Section

Samples of *cis*-polybutadiene, polyisobutylene, and smoked natural rubber were obtained from K. Schur of the BF Goodrich Co. A sheet of cured natural rubber (100 parts rubber plus 20 parts tetramethylthiuram disulfide) was obtained from J. Savoca of the BF Goodrich Co. The cured, carbon-black-filled *cis*-polybutadiene was the same as that examined previously using ^{13}C NMR with magic-angle spinning.[37]

Proton NMR images were obtained at ambient temperature at 200.1 MHz on a General Electric CSI-4.7 system with 33-cm room temperature horizontal bore. Samples up to 6 in. in diameter can be imaged on this system with the proper rf coil. Here a GE 3-in. diameter imaging coil was used. The maximum field-gradient strength was 2.0 G/cm. Spin-warp,[38] 2D FT images were obtained by using software available with the spectrometer. The rf carrier was placed midway between the two peaks in the spectrum of *cis*-polybutadiene and on resonance with the major ^1H peaks for the other polymers. Comparable images were obtained for *cis*-polybutadiene when the carrier was placed on the CH_2 resonance. Data from 256 individual phase-encode views were acquired as either a spin–echo or gradient–echo, sampled as 256 complex points in the frequency-encode or readout direction.

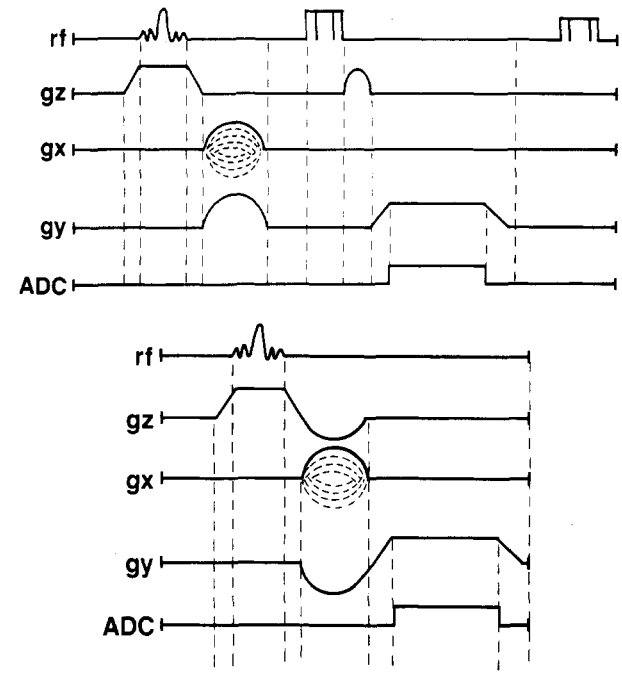

Figure 1. Top: spin-warp, spin–echo sequence for 2D FT NMR imaging. Bottom: gradient–echo sequence for 2D FT NMR imaging. TE is measured from the center of the selective pulse to the center of the gy readout gradient.

Figure 1, top, shows the basic spin–echo NMR imaging sequence used in this work. First, a nominally rectangular slice is excited by selective irradiation using a 2-ms, 90° rf pulse of sinc ($\sin x/x$) shape (with one lobe) in the presence of a field gradient. For axial slices (perpendicular to the B_0 field), the slice selection gradient is in the z direction as shown in Figure 1A. The sine-lobe-shaped, phase-encoding gradient (x direction, right–left) is stepped through 256 values from $-G_{max}$ to $+G_{max}$ to provide 256 echos or views. During the phase encoding, a dephasing gradient also is applied in the y direction (up–down). In the spin–echo sequence, a composite "hard" or broad-band 180° pulse (460 μs) is inserted to provide a spin echo at the center of the readout gradient. Each full echo is acquired as 256 complex points in the presence of the frequency encoding gradient during which time the analog-to-digital converter (ADC) is turned on. As expected, the intensity of this echo is determined by T_2, as field inhomogeneity and bulk susceptibility effects are refocused at the echo maximum. An additional dephasing gradient is inserted in z immediately after the 180° pulse. The final composite 180° pulse returns signal along the $-z$ axis back to the $+z$ axis in preparation for the next pulse train. The signal on the $-z$ axis is from regions unexcited during the initial selective excitation and inverted by the first 180° pulse, as well as z magnetization from the selected slice if less than a 90° selective pulse is used. The pulse sequence is repeated after 100 ms. In the spin–echo method, the minimum TE is determined by the length of several time periods, including the selective pulse width, gradient ramp times, the phase-encode time (3 ms), and the acquisition time. These latter two determine the field of view (FOV) in the image. For our FOV of 120 mm, slice thickness of 2 mm, and gradient strength, the minimum TE allowed is about 12 ms.

Figure 1, bottom, shows the gradient–echo pulse sequence used here. In this case the slice-selection gradient in z has a negative refocusing lobe to improve the slice profile. Even though the 180° pulse is not inserted, an echo is still produced by the two-lobe structure of the frequency encoding gradient. The initial, negative portion of this gradient dephases the spin vectors in the x, y plane. Upon sign reversal of the gradient, the spin vectors refocus at the point where the dephasing effects of the negative lobe are just canceled by the positive lobe. The echo then dephases again in the presence of the positive lobe of the readout gradient. Such an echo is called a gradient–echo. Its intensity is proportional to T_2^* (the apparent T_2, the time constant for decay of the free induction decay [FID]) because the effects of field inhomogeneity, chemical shift, and bulk susceptibility are not refocused. Given

Table I

	T_g (°C)	$10^9\tau_c$ (s)[a]	T_2 (ms)[b]	T_{2eff}* (ms)[e]	$\Delta\nu_{1/2}$ (Hz)[f]	T_1 (ms)
cis-polybutadiene[c]	−102	0.01	13	2.1	150	300, 390[g]
cis-polyisoprene[c] (natural rubber)	−70	0.4	9	1.0	310	380, 380[h]
polyisobutylene[d]	−70	20	<1	0.2	1650	
cured, filled *cis*-polybutadiene			4	0.4	740	250, 310[g]

[a] Average correlation time at 40–45 °C for backbone motion as determined by ^{13}C spin relaxation parameters. From ref 39. [b] Approximate, average proton T_2 determined as in the text. [c] For methine carbon. [d] For methylene carbon. [e] Effective T_2*, which includes the effects of bulk susceptibility broadening and contributions from different chemically shifted resonances, as for *cis*-polyisoprene, polyisobutylene, and the cured rubber. Derived from measured line width. [f] Of largest peak or band in spectrum, at half-height. [g] CH_2, CH. [h] $CH_2 + CH_3$, CH.

our conditions, the minimum TE allowed for the gradient–echo sequence is 6.4 ms. The two sequences, spin–echo and gradient–echo, can produce substantially different images for bulk polymers, as demonstrated below.

Approximate T_2's were measured by the Hahn spin–echo technique by turning off the phase-encoding gradient in the sequence in Figure 1, top, and following the echo intensity as a function of TE, the time to appearance of the echo. Effective T_2*'s were estimated from the line width in the standard FT spectrum ($T_2^* = 1/(\pi\Delta\nu_{1/2})$). In the cases where individual peaks are not resolved, the width at half-height of the entire band is taken. Approximate T_1's were measured by inversion–recovery.

Several images were obtained on a GE Signa clinical NMR imaging system at 64 MHz (1.5 T) using the 6-in. extremity coil provided. Samples up to 54 cm in diameter could be imaged on this system. Conditions were relaxed relative to those at 4.7 T. The maximum gradient strength was about 1 G/cm, a 3-mm slice was taken, and the field of view was 160 mm. One hundred twenty-eight phase-encode views were taken, and each echo was digitized in 256 points. All of this serves to increase the signal-to-noise ratio in the 64-MHz images relative to that at 200 MHz.

Results

In Table I is some pertinent information for the systems studied here. The three totally amorphous bulk polymers, which have low T_g's that are not drastically different from one another, have a range of over 3 orders of magnitude in backbone segmental mobility at ambient temperature. The backbone mobility can be represented by the average correlation time for segmental rotational motion, τ, which is given in Table I.[39] These correlation times were derived from ^{13}C spin-relaxation data. Also shown in Table I are the apparent T_2's measured by using the Hahn spin–echo method as described in the Experimental Section. The T_2's listed are least-squares fits of the total echo data to a single exponential. We did not measure T_2's of resolved, chemically shifted species. The value given for polyisobutylene is due primarily to the *gem*-dimethyl hydrogens, the value for the backbone CH_2 probably being considerably shorter. Approximate values of T_2*, the effective time constant for decay of the FID or echo, and T_1 are also given in Table I. The values indicate that all of our images are T_1 weighted in addition to T_2 or T_2* weighted.

In Figure 2, top, is the spin–echo image (TE = 12 ms) of a 2-mm slice of a block of bulk *cis*-polybutadiene. The actual polybutadiene block, 55 × 110 × 20 mm in size with irregularly shaped sides, is shown in Figure 3. The left side of the block contains a high density of trapped air bubbles or voids of about 1-mm diameter and less and hence visually appears translucent and somewhat milky. The right side contains few voids and is somewhat more transparent. Hence the block is a reasonable model of a manufactured rubber product with internal "defects". The block was placed with the long dimension along the bore of the magnet. The slice (Figure 2) is in the transverse (axial) plane in the region with a high density of voids. The outline of the image is a good representation of the cross

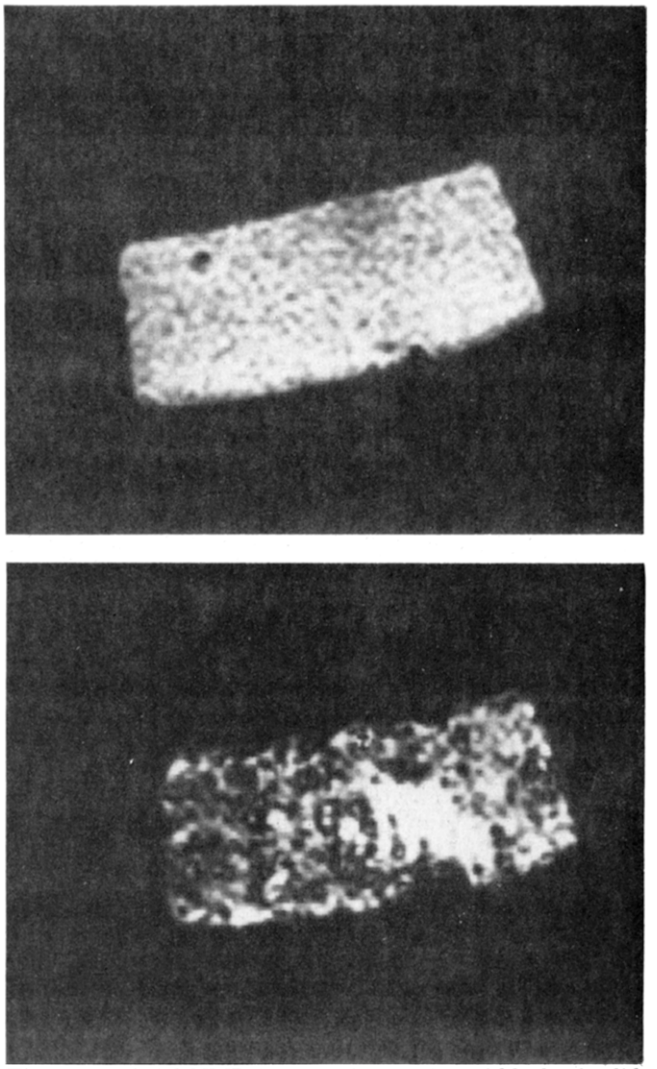

Figure 2. Axial NMR images of a portion of block of solid *cis*-polybutadiene (field of view, 120 × 123 mm; resolution, 256 × 256; shown is 20 × 55 mm face): top, spin–echo image (with TE of 12.0 ms; slice thickness, 2 mm; number of transients, 24); bottom, gradient–echo image (with TE of 6.4 ms; slice thickness, 1 mm; number of transients, 48).

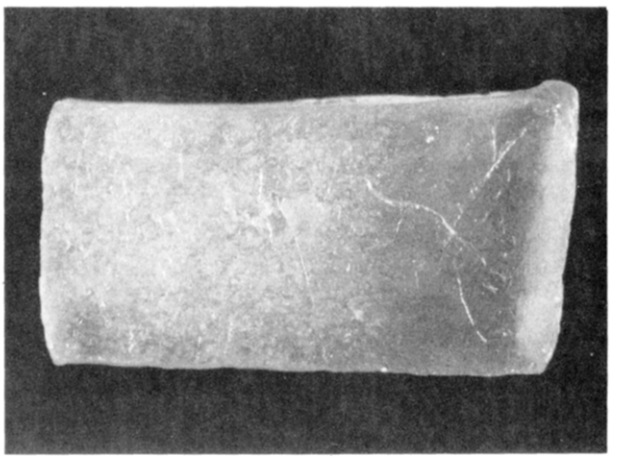

Figure 3. *cis*-Polybutadiene block studied here. The 110 × 55 mm face is shown. The void-free region is on the right.

section of the block at that point. Several defects, including two larger voids (upper left and lower right) and a low intensity region (upper right), are apparent. The image of Figure 2, top, was obtained in about $^1/_2$ h by using 24 repetitions per view. The mottled appearance, which occurs uniformly over most of the image, is attributed to the low signal-to-noise ratio of the image, although it may arise in part from many small voids.

In Figure 2, bottom, is the gradient–echo (TE = 6.4 ms) image through the same slice as the spin–echo image of Figure 2, top. Although the slice cross section is the same, the appearance of the gradient–echo image is considerably different from that of the spin–echo image. The gradient–echo image shows considerably more structure, that is, the presence of air bubbles or voids which in many instances appear reasonably well-defined in the image. Voids in the spin–echo image now appear larger, although this is obscured somewhat by major changes in the rest of the image. A bright area is also observed toward the center of the block. The origin of the bright area was not discovered visually but is evidently a void-free area.

We obtained good images of *cis*-polybutadiene on a Signa clinical imager at larger pixel size and slice thickness by using both spin–echo and gradient–echo sequences. Figure 4 shows images of *cis*-polybutadiene taken at 64 MHz in 1.4 h each. In Figure 4, top, is the spin-echo (TE = 14 ms) image of the block. The image is relatively uniform in intensity, except for the appearance of some well-defined voids in this slice. The outline of the block is well-defined. The parallel lines at the vertical edge of the block are truncation artifacts arising from the limited number of phase-encode views (128). The dark line at the top edge is a chemical shift artifact (see below). As expected, the image intensity drops at a TE of 35 ms (Figure 4, middle), but the uniformity remains, indicating no T_2 variations in the slice. Figure 4, middle, was acquired under identical conditions as Figure 4, top, and output at essentially the same display parameters. The major voids are still visible. The gradient–echo image (TE = 10 ms) (Figure 4, bottom) shows considerably more structure and the increased void density at the bottom. Moreover, all voids seen in the spin–echo image appear enlarged and more prominent in the gradient–echo image. The edge is also less well-defined in the gradient–echo image.

In Figure 5, top, is the spin–echo image of a 2-mm slice (TE = 11 ms) of a sample of smoked natural rubber. The sample, a 50 × 50 × 35 mm opaque block formed from 11 irregular vertical sheets of rubber fused together, but with some irregularly spaced gaps between several of the sheets, is shown in Figure 6. The spin–echo image has the mottled appearance seen for *cis*-polybutadiene, but with perhaps a slightly increased variation of intensity across the image. Several defects are apparent. Some evidence of the sheet structure is seen in the upper left corner. Figure 5, bottom, is the gradient–echo image of the same slice of the same sample. As for polybutadiene, the image is considerably different than the spin–echo image. The darkest regions of the spin-echo image correspond approximately to regions of essentially no signal in the gradient–echo image. The sheet structure is somewhat more evident in places by features running from upper right to lower left in the gradient-echo image. The bright, crosslike feature at top center of the block is a zero-frequency artifact at the exact center of the entire image. Because of the shorter T_2 and T_2* of natural rubber relative to *cis*-polybutadiene, it was necessary to take about 5 times as many averages to obtain a similar signal-to-noise ratio for the natural rubber.

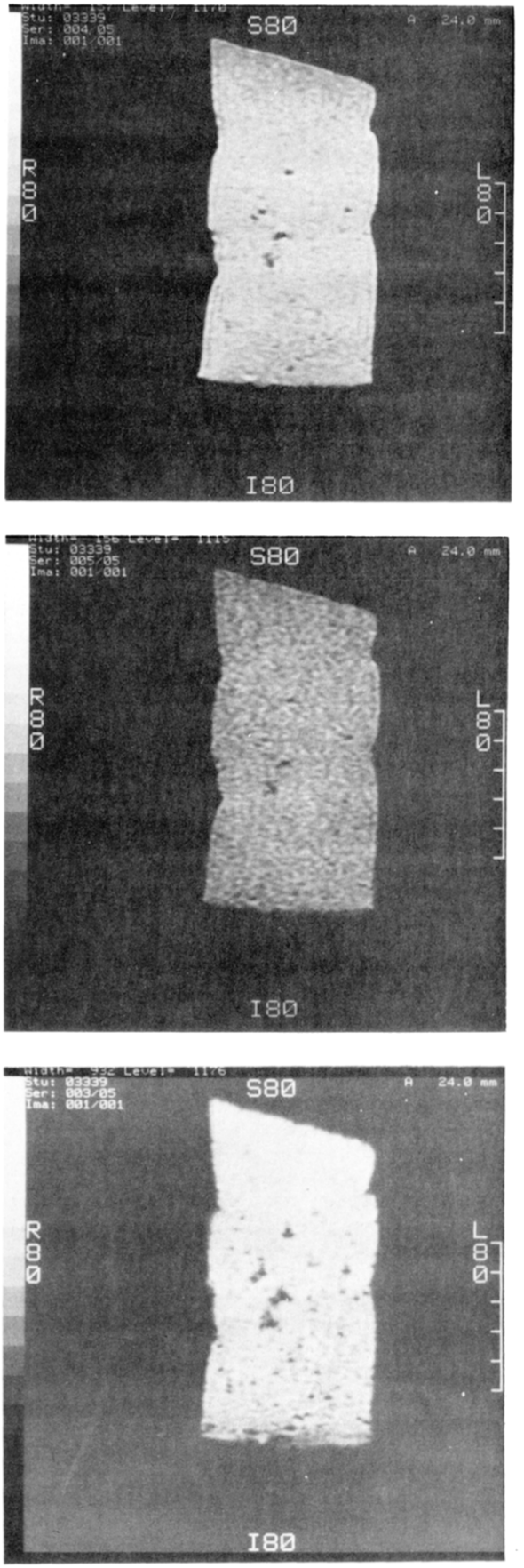

Figure 4. NMR images of the *cis*-polybutadiene block at 64 MHz (FOV, 16 cm; number of transients, 200; slice thickness, 3 mm; resolution, 128 × 256; TR, 200 ms). The 110 × 55 mm face is shown. The rf carrier was set to the methylene resource for these images: top, spin–echo (TE = 14 ms); middle, spin–echo (TE = 35 ms); bottom, gradient–echo (TE = 10 ms).

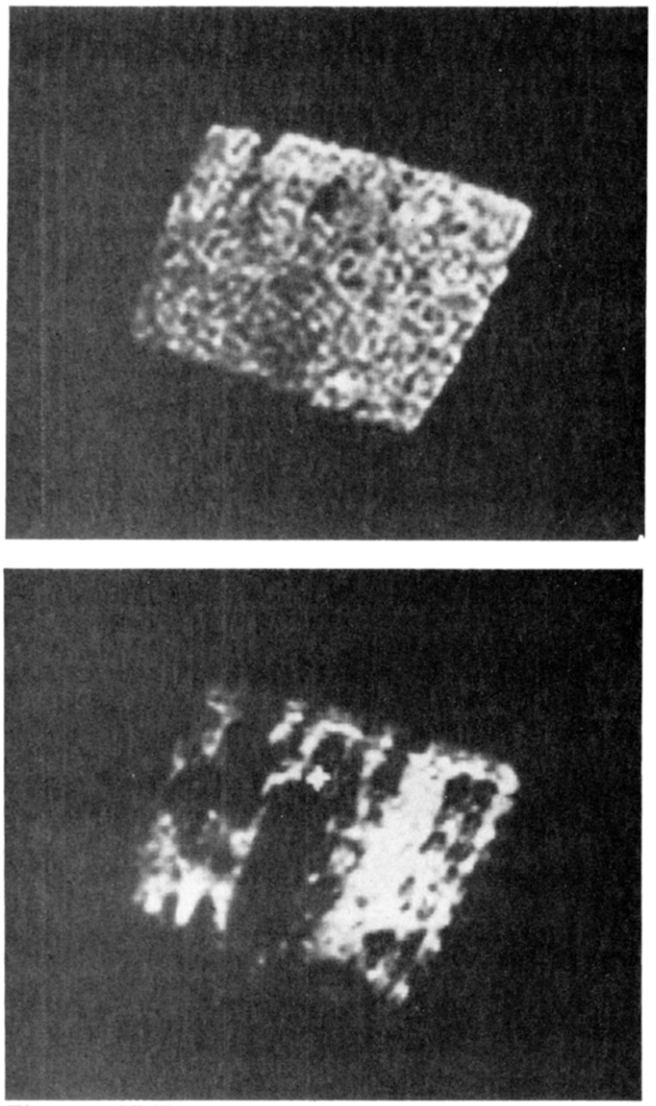

Figure 5. NMR images of a natural rubber sample (FOV, 120 × 123 mm; resolution, 256 × 256; shown is 35 × 50 mm face): top, spin–echo image with TE of 12 ms (slice thickness, 2 mm; number of transients, 120); bottom, gradient–echo image with TE of 6.4 ms (slice thickness, 2 mm; number of transients, 240).

Using the same conditions as for the samples above, we were not able to obtain an image for polyisobutylene. This is not surprising given the short T_2 of <1 ms for this rubber. By increasing the field of view and decreasing the resolution, we were able to shorten TE to 9 ms, allowing us to obtain a very weak spin–echo image after considerable signal averaging. The same was true for a sample of unfilled natural rubber cured extensively with tetramethylthiuram disulfide and with a T_g of −55 °C. No attempt at gradient–echo imaging of the above samples was made.

Figure 7 shows the spin–echo image of 10 sheets, each 2.0 mm thick, of a cured, carbon-black-filled *cis*-polybutadiene separated by glass spacers of variable thickness. The entire sample was held together tightly by several rubber bands. The smallest spacer is a sheet of paper approximately 0.07 mm in thickness, while the other spacers are, from left to right, 0.15, 0.30, 0.45, 0.60, 0.80, 1.0, 1.15, and 1.30 mm. Even though the T_2 of this sample is about 4 ms, we are still able to obtain a usable image in an overnight run with a TE of 12 ms. The low signal-to-noise ratio of the image arises in part from our choice of output level and window in the image. Level and window were chosen for maximum resolution of known features. The signal-to-noise ratio drops off at the bottom because the sample extends to the edge of the rf coil.

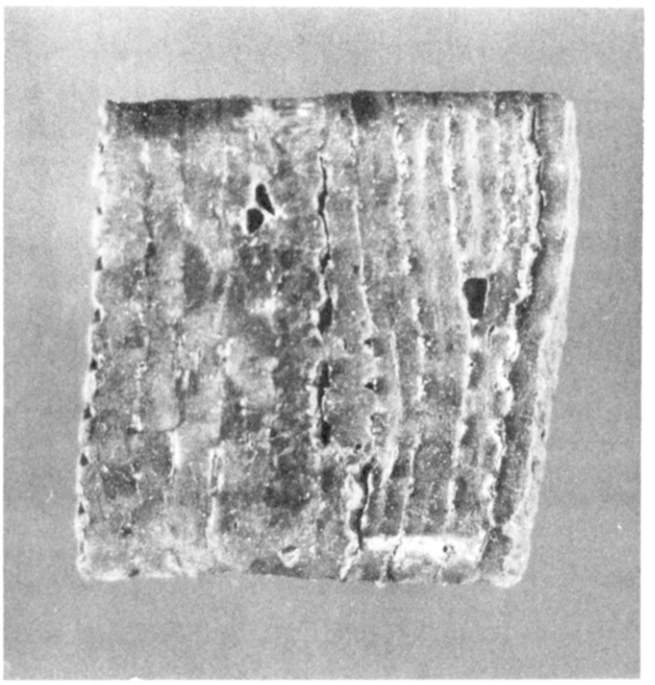

Figure 6. Natural rubber sample studied here. The 50 × 50 mm face is shown.

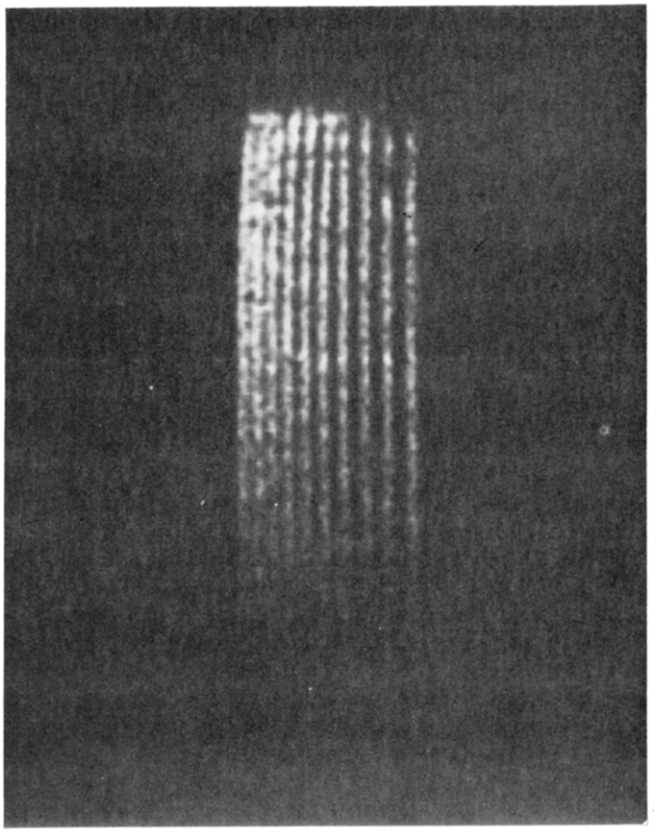

Figure 7. Spin–echo image of 10 sheets of a cured carbon-black-filled *cis*-polybutadiene (2.0-mm sheet thickness) separated by spacers of various thicknesses. The thicknesses of the spacers used are as follows (from left to right in mm): 0.07, 0.15, 0.30, 0.45, 0.60, 0.80, 1.0, 1.15, 1.30. The sample was placed with long dimension alone the z direction. The slice shown is in the y–z plane and 1.6 mm thick: field of view, 120 mm × 123 mm; resolution, 256 × 256, number of transients 240; TE, 12 ms. The signal intensity falls off at the bottom because the sample extends to the edge of the rf coil.

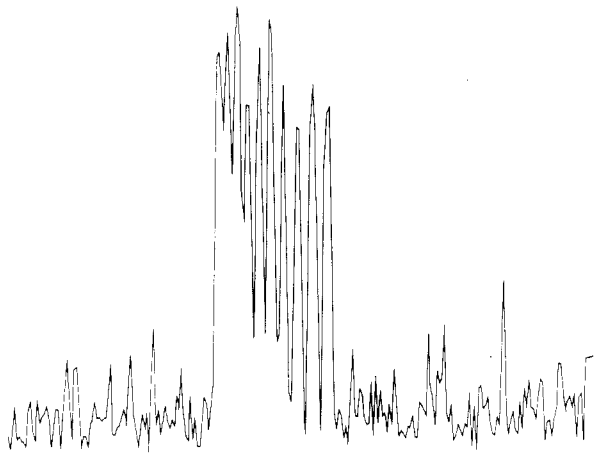

Figure 8. Horizontal profile (row 130) of the image in Figure 7. The profile demonstrates the signal-to-noise ratio obtained as well as the degree of resolution of the various rubber sheets at that point. The distance between the two rightmost peaks is about 3.3 mm.

Figure 8 shows a horizontal profile (row 130) of the data in Figure 7. This profile demonstrates the typical signal-to-noise ratio of the image, as well as the degrees of resolution between pairs of the various slices, each of which is a peak in Figure 8. We were not able to obtain a gradient–echo image of the filled sample under comparable conditions.

Discussion

Our results show that currently available NMR imaging techniques and equipment can be used to produce informative images of a range of elastomeric materials. Moreover, our work was performed on systems designed for large "samples". It is our belief that most industrial applications of NMR imaging will be performed on such systems, as opposed to high-field, small-sample systems. Highly rubbery, bulk polymers of low T_g and high-chain segmental mobility are easiest to image by using echo techniques. As chain motion slows and T_2 decreases, the images are of lower intensity and signal-to-noise ratio. At the TE's of 12–14 ms used here, polymers with T_2's of about 4 ms and above can be imaged with a spin–echo technique, although with varying degrees of difficulty. Polymers with T_2 on the order of 1 ms could not be imaged under our conditions.

We have demonstrated that cured, filled elastomers can be imaged successfully, as long as T_2 has not been shortened too much by the curing or filling process. It is known that a sizable portion of the line width in filled systems can be due to nonmotional factors such as bulk susceptibility.[36] Such nonmotional factors will be refocused in a spin–echo image and will not contribute to a loss of image intensity, although they will contribute to a loss of resolution. A more systematic study of the effects of curing and filling on elastomer images is necessary.

With the exception of a few obvious, large defects, the spin–echo images of Figures 2, top, and 5, top, appear somewhat uniform and mottled. The mottling is at the level of the pixel size. We cannot be sure whether it arises from voids, T_2 or T_1 differences, or the low signal-to-noise ratio of the image, although we feel that substantial T_2 or T_1 differences are unlikely and the low-signal-to-noise ratio is the most likely explanation.

On the other hand, the gradient–echo images of Figures 2, bottom, and 5, bottom, are relatively rich in detail. This detail for the most part cannot be due to T_2 effects or to direct absence of spin density due to voids because these would also be reflected in the spin–echo image. The detail probably arises from bulk-susceptibility variations in polymer at or near void surfaces or in regions of differing void density. The presence of a defect such as a void or NMR-transparent filler particle will generate a magnetic bulk susceptibility difference at the interface and presumably in regions close to the interface. Hence regions of the rubber near the surface of the defect may have shorter T_2*'s than the bulk rubber. In a gradient–echo image these surface regions would appear darker, enlarging the apparent size of the defect. The effect would be more pronounced at higher magnetic fields. Such an effect is observed at tissue-air boundaries in medical imaging by using gradient–echo sequences.[40]

Our low-field images in Figure 4 confirm the above interpretation. A number of well-defined voids are apparent in the spin–echo image of Figure 4, top. The presence of some of these voids was confirmed by visual examination of the block. Except for the major voids, the remainder of the spin–echo image is uniform. In the gradient–echo image (Figure 4, bottom) voids seen in the spin–echo image clearly appear enlarged. Also apparent in the gradient–echo image are many additional, smaller voids, particularly in the lower end of the block, where such voids are much more numerous.

Our results at 1.5 T are clearly superior to our results at 4.7 T. This is due to a number of factors including number of transients, FOV, slice thickness, resolution, and post-acquisition processing as well as the sensitivity of the two systems and the performance of their gradient hardware under our conditions. The differences also arise in part from the different magnetic field strengths of the two systems. There is currently a debate concerning the optimum B_0 field for NMR imaging of materials, particularly in the geophysical realm.[41] The tradeoff is between the increased sensitivity at higher field versus decreased resolution due to field dependent magnetic susceptibility broadening. We must emphasize strongly that *our results cannot be taken as evidence that lower fields are better for materials imaging*, although such may later be proved to be the case. The two instruments used here are considerably different in many performance characteristics. We have performed no proper study of the effect of B_0 field with all other conditions as constant as possible.

The spread of frequencies caused by the application of a linear field gradient G across a thickness Δx is $\gamma G \cdot \Delta x$. For hydrogen, the gyromagnetic ratio γ is 4258 Hz/G. To obtain a resolved image along x, it is necessary that the gradient-imposed spread in frequencies dominate the spread in frequencies due to the line width:

$$\gamma G \cdot \Delta x \gg \Delta \nu_{1/2}$$

Alternatively, one can calculate the size of the effect in the image that would be observed at a given line width.

Using bulk polybutadiene as an example, we can examine the various factors contributing to a loss of resolution. The largest is the chemical shift effect. The aliphatic and olefinic peaks of *cis*-polybutadiene are separated by about 660 Hz at 4.7 T, and each is about 150 Hz wide. The chemical shift separation results in a chemical shift artifact of 660 Hz/(2 G/cm·4258 Hz/G) = 0.78 mm. Examination of Figures 2 and 5 does not show the unambiguous presence of a chemical shift artifact at the edge of the block in the frequency-encode (vertical) direction. A clear chemical-shift artifact is seen in the low-field, spin–echo image of Figure 4, top (under these conditions, 0.5 mm).

The line width also influences the resolution of the images. The value of about 150 Hz for *cis*-polybutadiene at 4.7 T corresponds to a spatial uncertainty or "fuzziness"

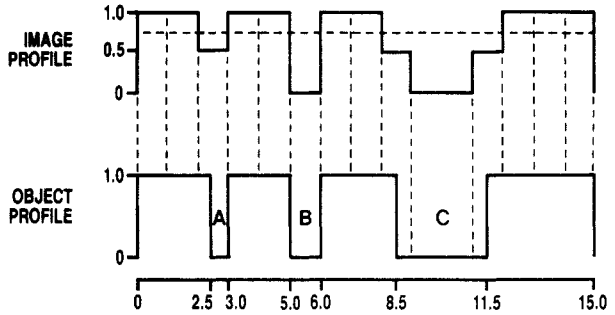

Figure 9. Profile of a hypothetical object and the expected NMR image profile at a pixel size of 1 mm in the linear dimension. Hole A, even though smaller than the pixel size, causes reduced NMR intensity for that pixel but appears wider than actual. Hole B is exactly 1 mm wide and is accurately represented. Hole C appears wider than actual. No account is taken of resolution losses due to the resonance line width or T_1 and T_2 differences in this idealization.

of 0.19 mm. Here this is less than the pixel size of 0.47 mm.

It is of interest to consider the resolution test in Figures 7 and 8 in more detail. Figure 7 has a 120-mm FOV in 256 points, giving a pixel size of 0.47 mm. Yet all nine spacers can be detected visually, even though the four smallest spacers are less than the pixel size. In fact, the boundary between the last two sheets can be detected even when the 0.07-mm spacer is removed. This seemingly anomalous behavior is readily explained by appeal to Figure 8. As mentioned previously, Figure 8 is a horizontal profile of the image, that is, the horizontal data slice at that point (slice 130). Most of the slices of the data in Figure 7 are similar to that in Figure 8. Generally it is assumed that, to resolve a particular feature, it must be larger than the pixel size. In our case that would mean resolving the spacer truly as a region of no NMR signal, that is, *to base line in the slice*. If the spacer is less than the pixel size, then the effect of the spacer is to reduce the intensity of the pixel at the point. Thus the two rubber sheets are resolved in the profile, but not to base line, for the smallest 7–8 pixels. If the image is displayed at a sufficiently high intensity threshold, the spacer is resolved.

A simple hypothetical example is shown in Figure 9. On the bottom is a hypothetical object profile and distance scale in mm. On the top is the corresponding image profile at a pixel size of 1 mm. Feature A, 0.5 mm wide, appears in the image profile as a 1-mm feature of reduced intensity. Feature B, exactly 1 mm wide, is truly represented in the image profile assuming that the pixel location corresponds exactly to that of the feature. Feature C is "widened" and will vary in size depending on the intensity threshold of image output.

We see from the profile in Figure 8 that only the largest 2–3 spacers are resolved to within noise level of the average baseline. The second spacer is 1.15 mm and the third spacer 1.0 mm wide. This result is reasonable if we consider that the pixel size is 0.47 mm, and the fuzziness due to the cured rubber line width is about 0.86 mm.

The implications of the above results need to be carefully considered as more attempts are made at resolving small features in solid polymers by NMR imaging. One important implication is that the effect of features considerably smaller than the pixel dimensions can be detected although the features cannot be truly resolved or well characterized. In Figure 7 the 0.07-mm paper spacer is detected as a slightly irregular band of reduced intensity. This smallest spacer is recognized in large part due to its regular features: i.e., it is a straight line. In general, one can say nothing about the size of features below the pixel size. This is because features of reduced intensity may arise from defects such as voids smaller than the pixel size, from a reduction of spin density over the whole pixel, or from T_1 or T_2 effects. This raises the possibility that a region of reduced intensity in a relaxation-time-weighted image may arise from the presence of defects smaller than the pixel size throughout the region and not from a difference in the relaxation time for that region. The magnification effect of bulk susceptibility variations will also contribute for gradient–echo images.

The results in Figures 7 and 8 illustrate a dilemma of NMR imaging of materials. A decision must be made as to intensity and contrast of the image. It may often be difficult or impossible to decide which combination of intensity and contrast yields an image "truly" representative of the morphology of the material. In our resolution test of known characteristics, examination of the profile at various points combined with the image itself yielded sufficient information for correct interpretation. However, for an unknown of identical characteristics, the above situation could not be distinguished readily from the situation where the six "gaps" on the left arise from T_2 differences in a continuous sample. Acquisition of several images of different T_2 weighting should yield a differentiation. If possible, increasing the resolution to the point where the feature of interest is highly resolved should also help, as would thinner slices. Of course, the signal-to-noise problem associated with small voxel sizes will limit how far these latter options can be carried.

It is also possible that part of our ability to detect such a small feature arises from reduced mobility and T_2 of the rubber at the surface of the sheet. This possibility is supported by the fact that the feature can be resolved even when the 0.07-mm sheet of paper is removed.

For the echo methods employed here, it will be necessary to shorten TE so as to recover most of the intensity of the echo signal and increase signal to noise. The minimum TE available in a particular situation is limited by factors such as the selective rf pulse width, gradient ramp times, the phase encode time, and the acquisition time. The value of TE can be lowered significantly only by decreasing the resolution or increasing the gradient strength. This assumes that the FID has not been lengthened by line-narrowing techniques. Another alternative is to collect half-echoes rather than full echoes to lower acquisition time, although an offsetting decrease in signal-to-noise ratio results. It may be that in this regard the projection–reconstruction technique is better suited to semirigid systems, as suggested previously.[19] Because thin slices are desirable, the 3D thick-slab technique may be useful.[42] Higher fields may be needed to provide the increased signal-to-noise necessary for observing smaller voxels, although chemical shift and magnetic susceptibility effects may limit this.

In conclusion, we have demonstrated that NMR imaging techniques can yield information concerning macroscopic defects in elastomeric systems. More work is necessary to define to what extent the image characteristics are influenced by factors such as B_0 field, gradient strength, polymer motion, cross-linking, filling, magnetic susceptibility, relaxation-time variations, and chemical shift effects.

Acknowledgment. We thank Dr. Ralph Hurd of GE NMR Instruments for invaluable assistance in obtaining some preliminary data at the GE applications lab. We also thank Ken Schur of BF Goodrich for providing the *cis*-polybutadiene, polyisobutylene, and natural rubber samples and Jackie Savoca of BF Goodrich for the sulfur-cured natural rubber.

Registry No. Polyisobutylene, 9003-27-4.

References and Notes

(1) Mansfield, P.; Morris, P. G. *Adv. Magn. Reson.* **1982**, Suppl. 2.
(2) Morris, P. G. *Nuclear Magnetic Resonance Imaging in Medicine and Biology*; Clarendon: Oxford, 1986.
(3) Gummerson, R. J.; Hall, C.; Hoff, W. D.; Hawkes, R.; Holland, G. W.; Moore, W. S. *Nature (London)* **1979**, *281*, 56.
(4) Baldwin, B. A. *SPE J.* **1984**, 39.
(5) Rothwell, W. P.; Vinegar, H. J. *Appl. Opt.* **1985**, *24*, 3969.
(6) Baldwin, B. A.; Yamanashi, W. S.; Lester, P. D. *Magn. Reson. Imaging* **1985**, *3*, 180.
(7) Hall, L. D.; Rajanayagam, V.; Hall, C. *J. Magn. Reson.* **1986**, *68*, 185.
(8) Vinegar, H. J. *JPT, J. Pet. Technol.* **1986**, *38*, 257.
(9) Maerefat, H. L.; Palmer, I.; Yamanashi, W. S.; Lester, P. D. *Magn. Reson. Imaging* **1986**, *4*, 122.
(10) Blackband, S.; Mansfield, P.; Barnes, J. R.; Clague, A. D. H.; Rice, S. A. *SPE Form. Eval.* **1986**, *1*, 31.
(11) Hall, L. D.; Rajanayagam, V. *J. Magn. Reson.* **1987**, *74*, 139.
(12) Wang, P. C.; Chang, S. J. *Wood Fiber Sci.* **1986**, *18*, 308.
(13) Hall, L. D.; Rajanayagam, V. *Wood Sci. Technol.* **1986**, *20*, 329.
(14) Hall, L. D.; Rajanayagam, V.; Stewart, W. A.; Steiner, P. R. *Can. J. For. Res.* **1986**, *16*, 423.
(15) Hall, L. D.; Rajanayagam, V.; Stewart, W.; Steiner, P. R.; Chow, S. *Can. J. For. Res.* **1986**, *16*, 684.
(16) Rothwell, W. P.; Holecek, D. R.; Kershaw, J. A. *J. Polym. Sci., Polym. Lett. Ed.* **1984**, *22*, 241.
(17) Rothwell, W. P.; Gentempo, P. P. *Bruker Rep.* **1985**, *1*, 46.
(18) Blackband, S.; Mansfield, P. *J. Phys. C: Solid State Phys.* **1986**, *19*, L49.
(19) Rothwell, W. P.; Tutunjian, P. W.; Vinegar, H. J., Proceedings of the Industry-University Cooperative Chemistry Program; Texas A&M University: College Station, TX, 1985.
(20) Suits, B. H.; White, D. *Solid State Commun.* **1984**, *50*, 291.
(21) Suits, B. H.; White, D. *J. Appl. Phys.* **1986**, *60*, 3772.
(22) Mansfield, P.; Grannell, P. K. *Phys. Rev. B* **1975**, *12*, 3618.
(23) Wind, R. A.; Yannoni, C. S. *J. Magn. Reson.* **1979**, *36*, 369.
(24) Garroway, A. N.; Baum, J.; Munowitz, M. G.; Pines, A. *J. Magn. Reson.* **1984**, *60*, 337.
(25) Szeverenyi, N. M.; Maciel, G. E. *J. Magn. Reson.* **1984**, *60*, 460.
(26) Emid, S. *Physica B+C (Amsterdam)* **1985**, *128B+C*, 79.
(27) Emid, S.; Creyghton, J. H. W. *Physica B+C (Amsterdam)* **1985**, *128B+C*, 81.
(28) Chingas, G. C.; Miller, J. B.; Garroway, A. N. *J. Magn. Reson.* **1986**, *66*, 530.
(29) Cho, H. M.; Lee, C. J.; Shykind, D. W.; Weitekamp, D. P. *Phys. Rev. Lett.* **1985**, *55*, 1923.
(30) De Luca, J.; Nuccetelli, C.; De Simone, B. C.; Maraviglia, B. *J. Magn. Reson.* **1986**, *67*, 169.
(31) McDonald, P. J.; Attard, J. J.; Taylor, D. S. *J. Magn. Reson.* **1987**, *72*, 224.
(32) Miller, J. B.; Garroway, A. N. *J. Magn. Reson.* **1988**, *77*, 187.
(33) Cory, D. G.; Reichwein, A.; van Os, J. W. M.; Veeman, W. S. Abstracts, 29th Experimental NMR Conference, Rochester, NY, April, 1988.
(34) See, for example, brochure entitled *Microscopy MRI Probes*: Product Literature, Doty Scientific: Columbia, SC 29223.
(35) Aguayo, J. B.; Blackland, S. J.; Schoeniger, J.; Mattingly, M.; Hintermann, M. *Nature (London)* **1986**, *322*, 190.
(36) Komoroski, R. A. In *High Resolution NMR Spectroscopy of Synthetic Polymers in Bulk*; Komoroski, R. A., Ed.; VCH Publishers: Deerfield Beach, FL, 1986; Chapter 4, p 121.
(37) Komoroski, R. A. *Rubber Chem. Technol.* **1983**, *56*, 959.
(38) Edelstein, W. A.; Hutchinson, J. M. S.; Johnson, G.; Redpath, T. *Phys. Med. Biol.* **1980**, *25*, 751.
(39) Komoroski, R. A.; Mandelkern, L. In *Applications of Polymer Spectroscopy*; Brame, E. G., Ed.; Academic: New York, 1978; Chapter 5.
(40) Haacke, E. M.; Bellon, E. M. In *Magnetic Resonance Imaging*; Stark, D. D., Bradley, W. G., Eds.; C. V. Mosby: St. Louis, 1988; Chapter 8, p 138.
(41) Dechter, J. J., ARCO Oil and Gas Co., private communication.
(42) Wehrli, F. W. In *Magnetic Resonance Imaging*; Stark, D. D., Bradley, W. G., Eds.; C. V. Mosby: St. Louis, 1988; Chapter 1, p 3.

Chain Mobility of Isotactic 1,4-*trans*-Poly(penta-1,3-diene) Included into Perhydrotriphenylene. A Broad-Line ^2H NMR Study

S. Brückner,* P. Sozzani,† C. Boeffel,‡ S. Destri,§ and G. Di Silvestro†

Dipartimento di Chimica del Politecnico di Milano, Piazza Leonardo da Vinci, 32, 20133 Milano, Italy, Dipartimento di Chimica Organica e Industriale, Universita di Milano, via Venezian 21, 20133 Milano, Italy, Max-Planck-Institut fur Polymerforschung, Jakob-Welder-Weg 11, D-6500 Mainz, FRG, and Istituto di Chimica delle Macromolecole del CNR, via E. Bassini, 15, 20133 Milano, Italy.

Received February 29, 1988; Revised Manuscript Received June 9, 1988

ABSTRACT: Deuteron NMR offers the possibility of studying local motions of polypentadiene chains included into a crystalline perhydrotriphenylene matrix. Results show the copresence of a rigid and a mobile fraction of C–D bonds, mobility ranging over a wide temperature interval, from 150 K up to 360 K (close to the melting point of the host compound). The relatively scarce effect of temperature is in agreement with a model where the chain mobility is primarily governed by steric interactions with a rigid host structure. A T_1 relaxation analysis indicates that a simple two-fraction model is an oversimplification, a better description requiring a more complex distribution of correlation times. A complete characterization of the samples assures for the absence of unreacted monomers and for the structure of the inclusion compound.

Introduction

Inclusion polymerization can be considered as a unique method for obtaining highly stereoregular polymers. The explanation is that they retain the crystal state ordering features of the inclusion adduct with the monomers. On this basis most works were oriented toward the detection of intramolecular and supermolecular order in the polymer, both native and after dissolution.[1]

In recent years more attention has been focused on the presence of disorder phenomena in crystalline polymers and in inclusion compounds as well. For example, in the case of inclusion polymerization, a considerable amount of monomer unit inversion has been detected in poly(isoprene) as obtained in perhydrotriphenylene (PHTP);

* Address correspondence to this author at Dipartimento di Chimica del Politecnico di Milano.
† Universita di Milano.
‡ Max-Planck-Institut fur Polymerforschung.
§ Istituto di Chimica delle Macromolecole del CNR.

0024-9297/89/2222-0607$01.50/0